Chinese Chemical Letters 33 (2022) 1430–1434

Contents lists available at ScienceDirect

Chinese Chemical Letters

journal homepage: www.elsevier.com/locate/cclet

Cascading V_2O_3/N-doped carbon hybrid nanosheets as high-performance cathode materials for aqueous zinc-ion batteries

Yue Niu[a,b,1], Denghui Wang[a,b,1], Yingjie Ma[a,*], Linjie Zhi[a,*]

[a] *CAS Key Laboratory of Nanosystem and Hierarchical Fabrication, CAS Center for Excellence in Nanoscience, National Center for Nanoscience and Technology, Beijing 100190, China*
[b] *University of Chinese Academy of Sciences, Beijing 100039, China*

ARTICLE INFO

Article history:
Received 28 June 2021
Revised 16 July 2021
Accepted 10 August 2021
Available online 16 August 2021

Keywords:
Aqueous zinc ion batteries
Cathode materials
Vanadium oxides
Nitrogen doped carbon
2D nanosheets
High performance

ABSTRACT

In recent years, especially when there is increasing concern about the safety issue of lithium-ion batteries (LIBs), aqueous Zn-ion batteries (ZIBs) have been getting a lot of attention because of their cost-effectiveness, materials abundance, high safety, and ecological friendliness. Their working voltage and specific capacity are mainly determined by their cathode materials. Vanadium oxides are promising cathode materials for aqueous ZIBs owing to their low cost, abundant resources, and multivalence. However, vanadium oxide cathodes still suffer from unsatisfactory capacity, poor stability, and low electrical conductivity. In this work, cascading V_2O_3/nitrogen doped carbon (V_2O_3/NC) hybrid nanosheets are prepared for high-performance aqueous ZIBs by pyrolyzing pentyl viologen dibromide (PV) intercalated V_2O_5 nanosheets. The unique structure features of V_2O_3/NC nanosheets, including thin sheet-like morphology, small crystalline V_2O_3 nanoparticles, and conductive NC layers, endow V_2O_3/NC with superior performance compared to most of the reported vanadium oxide cathode materials for aqueous ZIBs. The V_2O_3/NC cathode exhibits the discharge capacity of 405 mAh/g at 0.5 A/g, excellent rate capability (159 mAh/g at 20 A/g), and outstanding cycling stability with 90% capacity retention over 4000 cycles at 20 A/g.

Nowadays, with the rapid growth of electrical and electronic devices, especially electric vehicles, high-performance rechargeable batteries are urgently needed in worldwide [1]. Because of the high energy density, nonaqueous lithium-ion batteries (LIBs) have dominated the commercial rechargeable battery market [2]. However, the further development of LIBs is impeded by their weaknesses, including limited lithium resources [3], high-cost and particularly safety issues arising from toxic and flammable electrolytes. In contrast, aqueous zinc-ion batteries (ZIBs) do not suffer from these issues. Aqueous ZIBs have a great potential in large-scale energy storage applications because of their highly ambient stability, abundant resources, low cost, high safety, ecological friendliness, facile material processing and battery manufacturing [4,5]. As a result, various ZIBs have been fabricated and significant progresses have been made [6]. Unfortunately, there is still a great challenge in aqueous ZIBs due to lack of high-performance cathode materials [5,7–9]—cathode materials are critical to aqueous ZIBs because they offer Zn-storage sites and determine the working voltage and specific capacity of aqueous ZIBs [10]. Therefore, to achieve high-performance aqueous ZIBs, several kinds of cathode materials have been explored, including manganese-based oxides, vanadium-based oxides, Prussian blue analogues, olivine-based phosphates and sustainable quinone analogs [4].

Compared to other cathode materials, vanadium oxides and their derivatives have attracted more attention owing to their abundant resources, low cost, and multivalence of vanadium [11–21]. With vanadium oxides, such as V_2O_5 [17], V_2O_3 [22] and $V_3O_7 \cdot H_2O$ ($H_2V_3O_8$) [19], significant progress has been made in improving the performance of aqueous ZIBs. Nevertheless, most vanadium oxide cathode materials suffer from poor stability, low electrical conductivity, and unsatisfactory capacity. Thus, much effort on optimizing structures of vanadium oxides [14–17,22–25] and hybridizing them with conductive materials, such as amorphous carbon [26,27], porous carbon [28], nitrogen-doped carbon [29] and nitrogen-doped graphene [30], has been done to improve their stability, conductivity, and capacity in aqueous ZIBs [31–34]. However, the performance of vanadium oxide cathodes does not meet the demand of practical applications yet. It is still challenging

---

[*] Corresponding authors.
E-mail addresses: mayj@nanoctr.cn (Y. Ma), zhilj@nanoctr.cn (L. Zhi).
[1] These authors contributed equally to this work.

https://doi.org/10.1016/j.cclet.2021.08.058

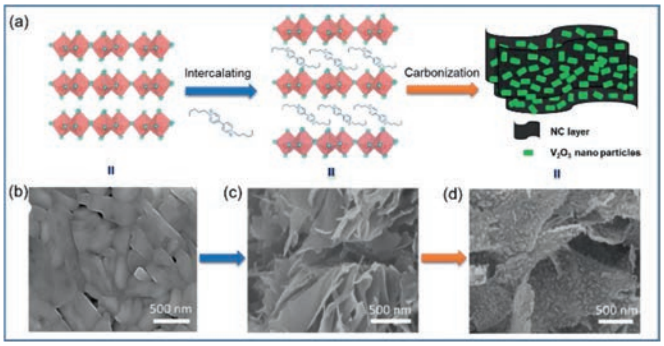

Fig. 1. (a) The synthetic procedure for the cascading V_2O_3/NC hybrid nanosheets. (b) SEM image of commercial V_2O_5. (c) SEM image of V_2O_5/PV. (d) SEM image of the cascading V_2O_3/NC hybrid nanosheets.

to achieve high-performance vanadium oxide cathodes for aqueous ZIBs.

Herein, we prepared a new kind of cascading V_2O_3/NC hybrid nanosheets by pyrolyzing pentyl viologen dibromide (PV) intercalated V_2O_5 nanosheets. During pyrolysis, viologen molecules were *in situ* carbonized into the 2D N-doped carbon (NC) layers and the V_2O_5 layers were reduced to crystalline V_2O_3 nanoparticles, which were intercalated into NC layers to form cascading V_2O_3/NC hybrid nanosheets. The thin sheet-like morphology of V_2O_3/NC enables to expose abundant electrochemical active sites for Zn ion storage, and the small crystalline V_2O_3 nanoparticles provide large accessible surface area for electrolytes and short path for Zn ion diffusion. Moreover, the conductive 2D NC layers facilitate the fast electron transfer as well as buffer the strain caused by volume change of the V_2O_3 nanoparticles during charge/discharge cycling. Consequently, as the cathode material in aqueous ZIBs, cascading V_2O_3/NC nanosheets delivery the significant discharge capacity of 405 mAh/g at 0.5 A/g and excellent rate capability (159 mAh/g at 20 A/g), and exhibit outstanding cyclic stability with 90% capacity retention over 4000 cycles at a high current rate of 20 A/g. The electrochemical performance of the V_2O_3/NC sheets is superior to most of the reported vanadium oxide cathodes for aqueous ZIBs [11].

As shown in Fig. 1, the cascading V_2O_3/NC hybrid nanosheets were fabricated through intercalating V_2O_5 with pentyl viologen dibromide followed by pyrolysis at 700 °C. V_2O_5 sheets possess the layered framework with large void space and contain plenty of high electronegative oxygen atoms that are favorable to bind cationic ions (Figs. 1a and c), both of which favor the insertion of cations into the interlayer of V_2O_5. Thus, when V_2O_5 nanosheets were dispersed in the aqueous solution of PV, the cationic viologens intercalated the interlayer of V_2O_5 to form the PV intercalated V_2O_5 (V_2O_5/PV), the driven force of which was the strong electrostatic interactions between the viologens and the lattice of V_2O_5 [35,36]. After intercalation, V_2O_5/PV kept the nanosheet-like morphology (Fig. 1c), but the interlayer space of V_2O_5 was expanded as indicated by the downshift of the (00l) XRD peak (Fig. S2 in Supporting information). And the content of viologens in V_2O_5/PV was measured as 27.8% by thermal gravimetric analysis (Fig. S3 in Supporting information).

After pyrolysis, the viologen molecules in the interlayer of V_2O_5 were carbonized into nitrogen doped carbon sheets (NC), and the intercalated V_2O_5 nanosheets (Fig. 1d) were reduced into V_2O_3 nanoparticles, giving the cascading V_2O_3/ NC hybrid nanosheets (Fig. 1d). The SEM spectrum of V_2O_3/NC shows that V_2O_3particles are embedded in the NC layers (Fig. 1d). The formation of NC was confirmed by Raman spectroscopy (Fig. 2a). The Raman spectrum of V_2O_3/NC shows that there are two obvious peaks at 1378 and 1587 cm^{-1}, corresponding to the characteristic D band and G band of carbon materials, respectively. And the diffraction peak of the product after pyrolysis is consistent with that of V_2O_3 (JCPDS No. 97–000–1875), confirming the conversion of V_2O_5 to V_2O_3 (Fig. 2d).

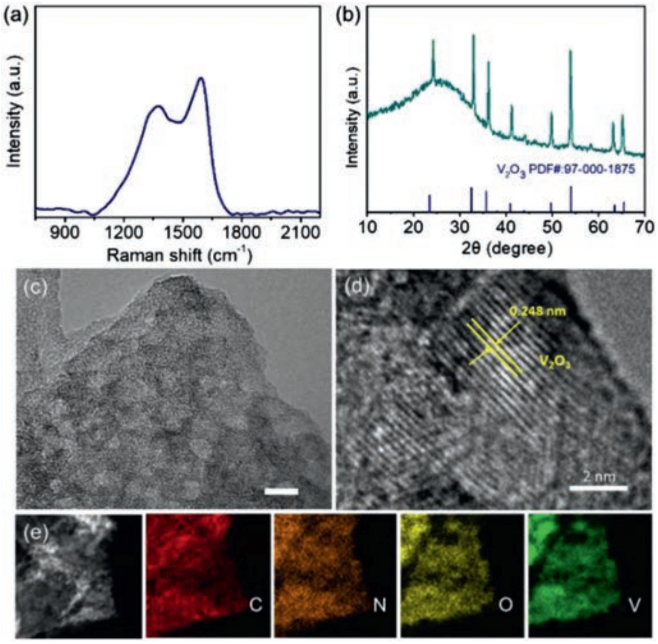

Fig. 2. (a) Raman spectrum, (b) XRD pattern (the lower is the standard pattern of V_2O_3, PDF #97–000–1875), (c) TEM image, (d) High-magnification TEM image and (e) energy-dispersive X-ray spectroscopy (EDS) maps of V_2O_3/NC.

The structure and composition of V_2O_3/NC were further characterized by the transmission electron microscope (TEM) (Fig. 2c). The TEM image also reveals that V_2O_3/NC features nanosheet-like morphology and V_2O_3 nanoparticles are inserted into the NC layers, forming cascading V_2O_3/NC hybrid nanosheets. High-resolution TEM analysis shows that V_2O_3 nanoparticles are highly crystalline with the lattice distance of 0.248 nm (Fig. 2d), corresponding to the (110) crystal plane of V_2O_3 (Fig. 2b) [30]. The composition of V_2O_3/NC were analyzed by element mapping, showing that there are four elements (V, O, N and C) in V_2O_3/NC and they are distributed homogeneously on the nanosheets (Fig. 2e).

The elemental composition of V_2O_3/NC nanosheets were analyzed in detail by X-ray photoelectron spectroscopy (Figs. 3a–d). The full XPS spectrum of V_2O_3/NC (Fig. 3a) reveals the presence of C, N, O and V, in accordance with the result of element mapping (Fig. 2e). The high-resolution C 1s spectrum (Fig. 3b) displays that there are four peaks at 284.5 eV, 285.6 eV, 287.4 eV and 289.0 eV, corresponding to C–C, C–N, C–O and O–C=O, respectively. The N 1s spectrum in Fig. 3c shows that there are four types of nitrogen, including pyridinic (399.1 eV), pyrrolic (400.4 eV), and graphitic (401.7 eV) types. The V 2p spectrum in Fig. 3d dexhibits four peaks at 515.9, 517.6, 523.3 and 524.9 eV arising from V $2p_{3/2}$ V^{3+}, V $2p^{3/2}$ V^{5+}, V $2p_{1/2}$ V^{3+} and V $2p_{1/2}$ V^{5+}, respectively. The existence of V^{5+} should come from partial surface oxidation of V_2O_3. To evaluate the content of NC in V_2O_3/NC and confirm its lamellar morphology, the V_2O_3/NC were immersed in a 3 mol/L HCl solution to remove the V_2O_3 nanoparticles. The TEM and SEM analyses (Fig. 3e and Fig. S5 in Supporting information) demonstrate that only NC remained and the V_2O_3 particles were removed completely after etching by HCl. The SEM image (Fig. 3f) shows that the remaining NC has nanosheet-like morphology as similar as the V_2O_3/NC nanosheets. By comparing the mass of the

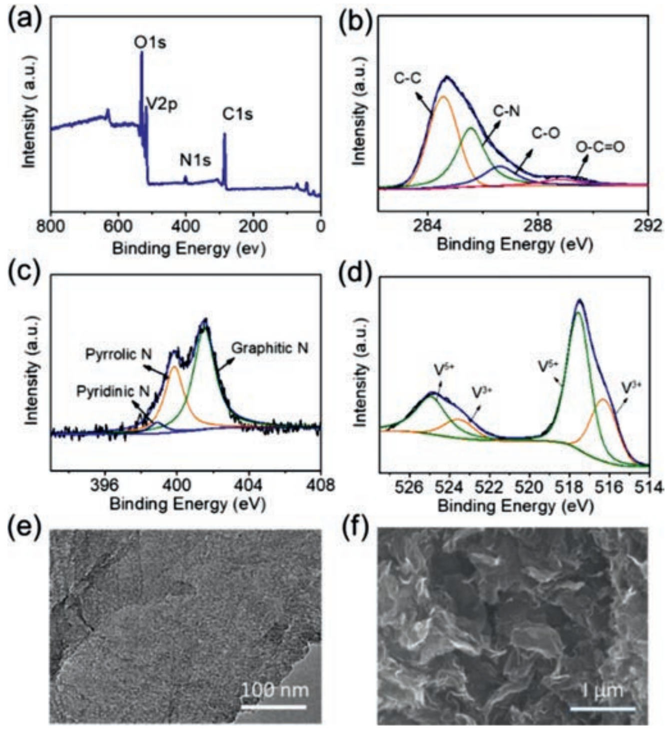

Fig. 3. (a) XPS analysis, (b) C 1s, and (c) N 1s and (d) V 2p spectra of the V_2O_3/NC hybrid nanosheets. (e) TEM and (f) SEM images of the NC nanosheets obtained by etching V_2O_3 particles from the V_2O_3/NC hybrid with a 3 mol/L HCl solution.

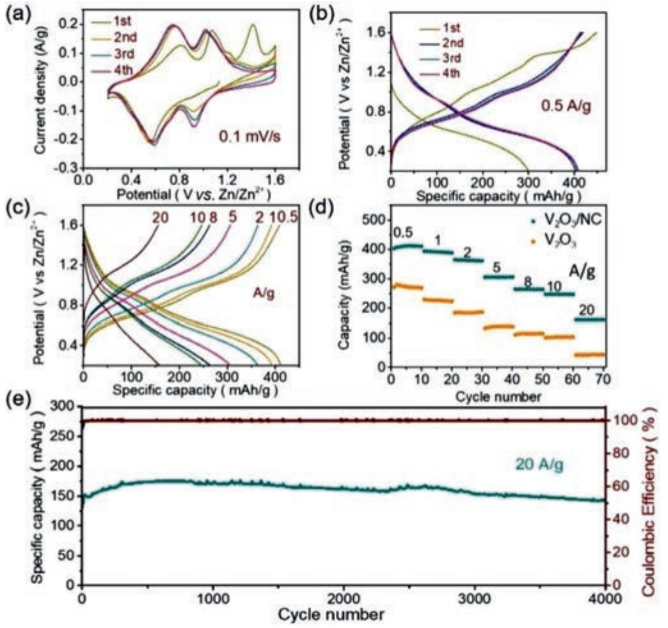

Fig. 4. (a) CV curves of V_2O_3/NC cathode in aqueous ZIBs at 0.1 mV/s. (b) GCD profiles of the Zn//V_2O_3/NC cell at 0.5 A/g. (c) GCD profiles of the Zn//V_2O_3/NC cell at different current densities ranging from 0.5 A/g to 20 A/g. (d) Rate performance of the Zn//V_2O_3/NC cell and the Zn//V_2O_3 cell. (e) cycling stability of the Zn//V_2O_3/NC cell at 20 A/g.

sample before and after acid-etching, the content of NC in V_2O_3/NC was measured as about 8.7 wt%. The above structure and composition analyses of V_2O_3/NC uncover that it possesses nanosheet-like morphology, and consists of V_2O_3 nanoparticles and conductive 2D nitrogen doped carbon sheets, which are layer-by-layer stacked to form the cascading hybrid nanosheets. The unique structure features of V_2O_3/NC nanosheets would enable them to achieve high-performance as cathode materials in aqueous ZIBs.

The electrochemical performances of V_2O_3/NC and V_2O_3 cathode in aqueous ZIBs were evaluated using coin cells with zinc foil anode and 3 mol/L aqueous Zn $(CF_3SO_3)_2$ electrolyte. The Zn//V_2O_3/NC (or V_2O_3) cells were performed in a voltage window of 0.4–1.6 V. The electrochemical behavior of V_2O_3/NC cathode was firstly investigated by cyclic voltammetry (CV) (Fig. 4a). The CV curve of the first cycle is quite different from that of the subsequent three cycles. Obviously, in the first cycle, there is an irreversible oxidation peak at about 1.4 V that disappears in the subsequent cycles, which should arise from the activation process of V_2O_3—the H_2O serves as a main reactant during the first electrochemical oxidation, and this process is expressed by the equation: $V_2O_3 + H_2O \rightarrow V_2O_{5-x}{\cdot}nH_2O + O_2 + H^+$ [37]. In follow-up cycles, there are two pairs of reversible redox peaks at 1.04/0.92 and 0.72/0.56 V, indicating the reversible two step Zn ion insertion and deinsertion behavior of V_2O_3/NC cathode, respectively [19,20].

The galvanostatic charge-discharge (GCD, Fig. 4b) profiles illustrate that the discharge specific capacity of Zn//V_2O_3/NC cell increased from 300 mAh/g to 405 mAh/g after activating at 0.5 A/g in the first cycle and then remained 405 mAh/g in the following charge/discharge cycles. Compared to most of the vanadium oxide cathodes (Table S1 in Supporting information), the high specific capacity (405 mAh/g at 0.5 A/g) makes V_2O_3/NC cathode more competitive in aqueous ZIBs. Such extraordinary specific capacity is mainly attributed to the distinctive structure of V_2O_3/NC nanosheets, where the sheet-like morphology of V_2O_3/NC enables to expose abundant electrochemical active sites for Zn ion storage. As a result, a superior energy density of 367 Wh/kg with a power density of 0.45 kW/kg was obtained for V_2O_3/NC cathode materials, which surpasses that of most reported vanadium oxide cathodes [6]. Notably, the H^+ intercalated reaction, which contributes to the capacity of the cell as well, exists in most acid ZIBs. Thus, the contribution of H^+ intercalation to the electrochemical capacity was identified by an additional GCD measurement through a three-electrode configuration in dilute H_2SO_4 (pH $\approx$ 4) at a current density of 0.5 A/g (Fig. S6 in Supporting information). H^+ intercalation releases an ultralow specific capacity of 23 mAh/g at 0.5 A/g, and such negligible contribution indicates that the Zn^{2+} intercalation mechanism dominates in V_2O_3/NC based ZIBs.

The rate capability of Zn//V_2O_3/NC cell was estimated at different current densities ranging from 0.5 to 20 A/g (Figs. 4c and d). It can be observed that the V_2O_3/NC cathode releases the discharge specific capacities of 405, 393, 362, 305, 263, 246 and 159 mAh/g at current densities of 0.5, 1.0, 2.0, 5.0, 8.0, 10.0 and 20.0 A/g, respectively. It is known that vanadium oxide cathodes for ZIBs suffer from low electrical conductivity and slow Zn^{2+} diffusion caused by the strong electrostatic interaction between Zn^{2+} and the lattice of vanadium oxides, leading to poor rate performance [4]. In contrast, V_2O_3/NC cathode possesses excellent rate performance as it still has the discharge specific capacity as high as 159 mAh/g at high current density of 20.0 A/g, which is superior to most of the vanadium oxide cathodes [9,10,38]. The outstanding rate capability should arise from the unique structure of V_2O_3/NC hybrid nanosheets. The sheet-like morphology of V_2O_3/NC and the small crystalline V_2O_3 nanoparticles provide large accessible surface area for electrolytes, reducing the resistance of the electrode/electrolyte interface. Besides, the small crystalline V_2O_3 nanoparticles provide short path for Zn ion diffusion, relieving the sluggish Zn^{2+} diffusion. Moreover, the conductive NC layers enable V_2O_3/NC to have good electron conductivity and the aqueous electrolyte offers remarkable ionic conductivity [4], both of which benefit the high-rate performance. In addition, the nitrogen in NC layer would enhance the affinity of V_2O_3/NC cathode towards electrolytes, con-

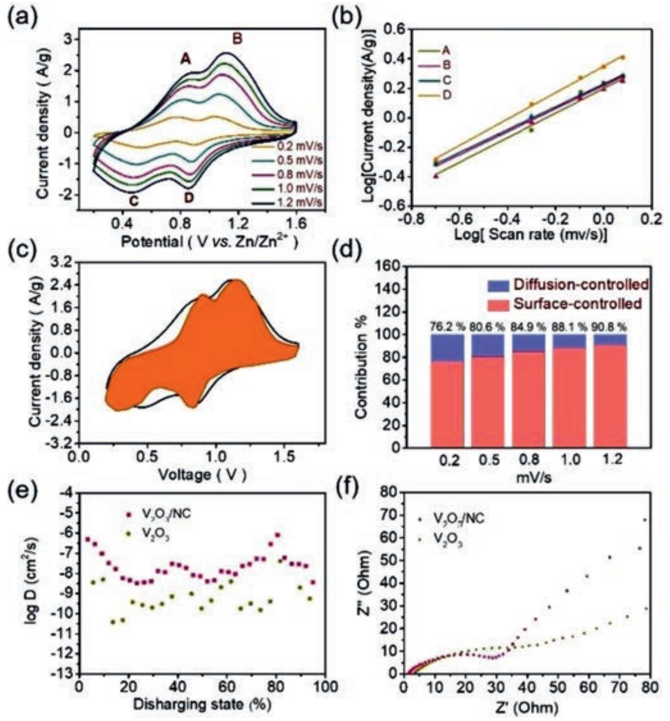

Fig. 5. (a) CV curves of Zn//V_2O_3/NC cell at different scan rates. (b) log(*i*) *vs.* log(*v*) curves of cathodic and anodic peaks. (c) CV curve with capacity separation at 1.2 mV/s. (d) The surface-controlled contribution ratios at multiple scan rates. (e) Zn^{2+} diffusion coefficients during the discharging process of V_2O_3/NC and V_2O_3. (f) Nyquist plots of V_2O_3/NC and V_2O_3 based ZIBs.

tributing the high-rate capability as well. On the contrary, compared to V_2O_3/NC, the bulky V_2O_3 cathode material that was also synthesized by annealing V_2O_5 particles demonstrates much lower capacities at different current densities (Fig. 4d and Fig. S9 in Supporting information). The superior electrochemical performance of V_2O_3/NC compared with V_2O_3 highlights the role of the unique structure of V_2O_3/NC in achieving high performance ZIBs. Besides, N_2 adsorption−desorption isotherm analysis demonstrates that V_2O_3/NC possesses much higher specific surface area compared to V_2O_3 (58.2 m^2/g *vs.* 18.4 m^2/g, Figs. S4 and S7 in Supporting information), which contributes to its superior performance as well.

Additionally, V_2O_3/NC cathode exhibits outstanding cycling stability as it maintains a discharge capacity of 144 mAh/g after 4000 cycles at a high current density of 20 A/g, suppressing most of the reported vanadium oxide cathode materials [8]. The long cycle life should arise from the cascading framework, where the conductive NC layers buffer the strain caused by volume change of the V_2O_3 nanoparticles during charge/discharge cycling. It should be noted that the zinc anode keeps stable during cycling test, although lots of leaf-like zinc dendrite was observed on the surface zinc anode after cycling (Fig. S8 in Supporting information).

To further explore the Zn ion storage behavior of V_2O_3/NC cathode, we investigated the electrochemical kinetics in the Zn//V_2O_3/NC cell by CV test with increasing scan rates from 0.2 mV/s to 1.2 mV/s. When increasing the scan rate (Fig. 5a), the CV curves almost remain unchanged, implying the good rate performance. The dominated kinetic process of the Zn//V_2O_3/NC cell during charge/discharge can be evaluated by the *b* value in the equation $i = av^b$. Theoretically, $b = 0.5$ represents the diffusion-controlled insertion process, while $b = 1$ indicates the surface-controlled process. As shown in Fig. 5b, the *b* values of the four peaks (A, B, C and D) are 0.89, 0.99, 0.95 and 0.97, respectively, indicating that Zn ion storage in the Zn//V_2O_3/NC cell is dominated by the surface-controlled process but not the Zn^{2+} ion diffusion. The behavior should be due to the short path for Zn ion diffusion arising from the small crystalline V_2O_3 nanoparticles. We evaluated the surface-controlled contribution at different scanning rates. At a scan rate of 1.2 mV/s, the shaded area stands for the surface-induced capacity, accounting for 90.8% of the total capacity (Fig. 5c). Similar capacity separation curves at other four scan rates are exhibited in Fig. S10 (Supporting information). The contribution ratios of surface-controlled mechanism at different scan rates are calculated and displayed in Fig. 5d. These results display that the surface-controlled contribution ratio increases from 76.2% to 90.8% as the scan rate rises from 0.2 mV/s to 1.2 mV/s, demonstrating that this process gradually dominates kinetic process of the Zn//V_2O_3/NC cell as the scan rate raise.

Galvanostatic intermittent titration technique (GITT) was adopted to further investigate Zn^{2+} solid state diffusion kinetics in V_2O_3/NC or V_2O_3 during the discharging process. The diffusion coefficient of V_2O_3/NC during the cycles ranges from 3.7×10^{-9} cm^2/s to 4.7×10^{-7} cm^2/s (Fig. 5e), which is almost an order of magnitude higher than that of V_2O_3 in the range of 5.6×10^{-10}–3.3×10^{-9} cm^2/s. Moreover, electrochemical impedance spectroscopy (EIS) was performed to investigate the ion and electron conductivities of V_2O_3/NC and V_2O_3 cathodes. Nyquist plots of V_2O_3 electrode and V_2O_3/NC after the first cycle are shown in Fig. 5f. The intercept at high frequency is associated with innate resistance (R_s). The semicircle at high frequency relates to the charge transfer resistance (R_{ct}) at the electrolyte/electrode interface. The sloped line at low frequency (Warburg impedance) is attributed to Zn^{2+} diffusion in the electrode. Compared to V_2O_3, V_2O_3/NC possesses smaller R_s (1.7 *vs.* 3.5 Ω), which might be due to the cascading structure of V_2O_3/NC and conductive 2D NC sheets. The R_{ct} of V_2O_3/NC is also smaller than that of V_2O_3 (27.5 *vs.* 40.6 Ω) and thus V_2O_3/NC has more efficient charge transfer process, which should arise from larger accessible surface area of V_2O_3/NC for electrolytes. Additionally, the slope of V_2O_3/NC is higher than that of V_2O_3, implying that the unique structure of V_2O_3/NC provides better Zn^{2+} diffusion capability. Both results of GITT and ESI demonstrate that the unique structure features of V_2O_3/NC give it efficient ion and electron conductivities, which further leads to extraordinary rate capability.

In summary, to achieve high-performance ZIBs with vanadium oxide cathodes, we have fabricated the cascading V_2O_3/NC hybrid nanosheets by pyrolyzing pentyl viologen dibromide (PV) intercalated V_2O_5 nanosheets. V_2O_3/NC hybrid nanosheets bear unique structure features, including the nanosheet-like morphology, the cascading framework, small crystalline V_2O_3 nanoparticles, and conductive NC layers. All the features are beneficial to alleviating the problems of vanadium oxide cathodes for aqueous ZIBs, such as unsatisfactory capacity, poor stability, and low electrical conductivity. Therefore, this V_2O_3/NC cathode delivers the competitive electrochemical performance compared to the best reported vanadium oxide cathodes for aqueous ZIBs (Fig. S6) [5]. This work will contribute to developing high-performance transition metal oxides/carbon composites for zinc ion storage.

Declaration of competing interest

The authors declare that they have no known competing financial interests or personal relationships that could have appeared to influence the work reported in this paper.

Acknowledgments

We gratefully acknowledge funding support from the Ministry of Science and Technology of China (No. 2012CB933403), Beijing

Natural Science Foundation (No. 2182086) and the National Natural Science Foundation of China (Nos. 51425302, 51302045).

Supplementary materials

Supplementary material associated with this article can be found, in the online version, at doi:10.1016/j.cclet.2021.08.058.

References

[1] Z. Yang, J. Zhang, M.C. K.intner Meyer, et al., Chem. Rev. 111 (2011) 3577–3613.
[2] B. Liu, J.G. Zhang, W. Xu, Joule 2 (2018) 833–845.
[3] J.B. G.oodenough, Y. Kim, J. Power Sources 196 (2011) 6688–6694.
[4] G. Fang, J. Zhou, A. Pan, et al., ACS Energy Lett. 3 (2018) 2480–2501.
[5] M.E. P.am, D. Yan, J. Yu, et al., Adv.Sci. 8 (2020) 2002722.
[6] A. Konarov, N. Voronina, J.H. J.o, et al., ACS Energy Lett. 3 (2018) 2620–2640.
[7] L.R. D.e Jesus, J.L. A.ndrews, A. Parija, et al., ACS Energy Lett. 3 (2018) 915–931.
[8] L. Chen, Q. An, L. Mai, Adv. Mater. Interfaces 6 (2019) 1900387.
[9] B. Yong, D. Ma, Y. Wang, et al., Adv. Energy Mater. 10 (2020) 2002354.
[10] N. Zhang, X. Chen, M. Yu, et al., Chem. Soc. Rev. 49 (2020) 4203–4219.
[11] L. Fan, Y. Ru, H. Xue, et al., Adv. Sustain. Syst. 4 (2020) 2000178.
[12] Z. Liu, H. Sun, L. Qin, et al., ChemNanoMat 6 (2020) 1553–1566.
[13] S. Natarajan, S.J. Kim, V. Aravindan, J. Mater. Chem. A 8 (2020) 9483–9495.
[14] M. Yan, P. He, Y. Chen, et al., Adv. Mater. 30 (2018) 1703725.
[15] Y. Yang, Y. Tang, G. Fang, et al., Energy Environ. Sci. 11 (2018) 3157–3162.
[16] F. Liu, Z. Chen, G. Fang, et al., Nano Micro Lett. 11 (2019) 25.
[17] F. Ming, H. Liang, Y. Lei, et al., ACS Energy Lett. 3 (2018) 2602–2609.
[18] J. Ding, Z. Du, B. Li, et al., Adv. Mater. 31 (2019) e1904369.
[19] P. He, Y. Quan, X. Xu, et al., Small 13 (2017) 1702551.
[20] P. Hu, T. Zhu, X. Wang, et al., Nano Lett. 18 (2018) 1758–1763.
[21] M.H. A.lfaruqi, V. Mathew, J. Song, et al., Chem. Mater. 29 (2017) 1684–1694.
[22] H. Luo, B. Wang, F. Wang, et al., ACS Nano 14 (2020) 7328–7337.
[23] L. Ma, N. Li, C. Long, et al., Adv. Funct. Mater. 29 (2019) 1906142.
[24] L. Ma, S. Chen, C. Long, et al., Adv. Energy Mater. 9 (2019) 1902446.
[25] S. Deng, Z. Yuan, Z. Tie, et al., Angew. Chem. Int. Ed. 59 (2020) 22002–22006.
[26] H. Wu, Z. Zhang, M. Qin, et al., J. Am. Ceram. Soc. 103 (2020) 2643–2652.
[27] H. Chen, Y. Rong, Z. Yang, et al., Ind. Eng. Chem. Res. 60 (2021) 1517–1525.
[28] Y. Ding, Y. Peng, S. Chen, et al., ACS Appl. Mater. Interfaces 11 (2019) 44109–44117.
[29] H. Zhang, Z. Yao, D. Lan, et al., J. Alloys Compd. 861 (2021) 158560.
[30] J. Zhang, Q. Li, Z. Liao, et al., ChemElectroChem 5 (2018) 1387–1393.
[31] D. Xie, F. Hu, X. Yu, et al., Chin. Chem. Lett. 31 (2020) 2268–2274.
[32] X. Liu, Y. Fang, P. Liang, et al., Chin. Chem. Lett. 32 (2021) 2899–2903.
[33] R. Hu, Y. Fang, X. Liu, et al., Chem. Res. Chin. Univ. 37 (2021) 311–317.
[34] F. Cui, J. Zhao, D. Zhang, et al., Chem. Eng. J. 390 (2020) 124118.
[35] T. Nakato, I. Kato, K. Kuroda, et al., J. Colloid Interface Sci. 133 (1989) 447–451.
[36] I. Kato, T. Nakato, K. Kuroda, et al., Colloids Surf. 49 (1990) 241–245.
[37] H. Luo, B. Wang, F. Wang, et al., ACS Nano 14 (2020) 7328–7337.
[38] B. Tang, L. Shan, S. Liang, et al., Energy Environ. Sci. 12 (2019) 3288–3304.